



Slurry Erosion–Corrosion Resistance of MoNbTaTiZr High Entropy Alloy

A. K. Sharma¹ · G. Perumal¹ · H. S. Arora¹ · H. S. Grewal¹

Received: 6 February 2021 / Revised: 27 April 2021 / Accepted: 2 May 2021 / Published online: 16 May 2021
© The Author(s), under exclusive licence to Springer Nature Switzerland AG 2021

Abstract

Slurry erosion–corrosion is a severe issue for many engineering components used in marine, petrochemical, and agricultural sectors. The deleterious effects of the slurry erosion–corrosion significantly lower the service life and enhance the maintenance cost. For limiting the slurry erosion–corrosion effects, there is a need for high-performance advanced materials. In the present work, equimolar MoNbTaTiZr high-entropy alloy (HEA) was developed, and its slurry erosion–corrosion behavior was investigated. For comparison, conventionally used stainless steel SS316L was also investigated. The detailed microstructural characterization showed the presence of a two-phase bcc crystal structure in the HEA. The major bcc phase was predominantly composed of Ta, Mo, and Nb with the interdendritic region being rich in Ti and Zr. The MoNbTaTiZr HEA showed 2 times higher hardness than the SS316L steel. Under slurry erosion–corrosion condition, the HEA showed 3.5 times higher resistance while under erosive conditions, two times better performance than the reference material. The analysis of the eroded surface morphology showed the presence of a mixed ductile–brittle erosion response for the HEA. The improved performance of the HEA is predominantly related to the high hardness and extremely high corrosion resistance. Electrochemical corrosion testing revealed that the HEA has 80 times lower current density than SS316L and high pitting resistance, resulting in low corrosion rates. The electrochemical impedance spectroscopy (EIS) findings showed a denser and highly stable passive layer. The results indicated that MoNbTaTiZr HEA could be effectively used for countering the slurry erosion–corrosion and corrosive conditions.

Keywords Erosion–corrosion · High-entropy alloy · Corrosion · Slurry erosion

1 Introduction

Slurry erosion is a detrimental phenomenon leading to surface degradation in hydraulic machinery. Slurry erosion when combined with corrosion creates a synergistic effect leading to a substantial loss of material and thus in turn reducing its reliability. It is a serious concern in many industries including oil and gas, mining, sewage treatment facility, paper recycling facilities, and hydroelectric power owing to their harsh operating conditions [1, 2]. Slurry erosion and corrosion can cause significant damage to components such as propellers, pumps, valves, and pipelines resulting in a

significant decrease in components life and thereby creating serious economic impact. Slurry erosion–corrosion has concerned many researchers in recent years and encouraged them to tackle this barrier by utilizing different advanced materials and engineering them based on required working conditions [3, 4]. In this context, the recently developed high-entropy alloys (HEAs) with exceptional properties have shown promising results.

High entropy alloys (HEAs) consist of five or more elements in equivalent or almost equal amounts, with atomic fractions ranging from 5 to 35% [5]. The pioneering work by Brian Cantor and Jien–Wei–Yeh in 2004 ignited research on this untouched field, and since then, many alloy systems have been studied to identify HEA systems with an enhanced combination of properties, leading to the extraordinary growth of this field [6, 7]. HEA may contain minor elements with an atomic fraction of less than 5%. The principle of HEA is based on the fact that high entropy of mixing can lead to the formation of a stable single-phase solid solution rather than an intermetallic formation. The most

✉ H. S. Arora
harpreet.arora@snu.edu.in

✉ H. S. Grewal
harpreet.grewal@snu.edu.in

¹ Surface Science and Tribology Lab, Department of Mechanical Engineering, Shiv Nadar University, Gautam Budh Nagar, India

commonly formed single-phase solid solution is face-centered cubic (fcc), body-centered cubic (bcc), and hexagonal close-packed (hcp) structure. Four core effects: high configurational entropy, sluggish diffusion, lattice distortion, and cocktail, effect account for their promising mechanical properties including high strength, excellent resistance to high-temperature softening and creep, high fatigue strength, and good tribological properties [5, 6]. Due to the aforementioned mechanical properties, HEA has placed itself as a potential leader in the alloy segment for marine applications [8], high-temperature application [9], energy conversion and storage [10], nuclear application [11] as well as bioimplant material for the healthcare industry [12].

The first single-phase HEA CrMnFeCoNi has become the benchmark material as it exhibits exceptional low-temperature mechanical properties and high fracture toughness [13]. Similarly, VNbMoTaW shows high compression yield strength of 600 MPa even at a temperature of 1400 °C, which exceeds that of conventional superalloys such as Inconel-718 [14, 15]. Though a limited amount of literature is available regarding the tribological behavior of HEA, there are few focused studies on slurry erosion and corrosion behavior of bulk HEA and coatings. Nair et al. [8, 16] reported a superior slurry erosion resistance of $Al_{0.1}CoCrFeNi$ HEA when compared to that of mild steel at a normal angle despite having lower hardness (2/3rd of mild steel). The bulk HEA showed significantly higher corrosion resistance than SS316L. Further, in the later investigation, the microwave-derived coatings of $Al_xCoCrFeNi$ ($x=0.1, 1, 3$) on SS316L substrate showed nearly three times lower erosion rate at an oblique angle, while under normal impingement, equimolar composition showed better performance than their non-equimolar counterparts [17]. The equimolar composition showed better erosion resistance than the non-equimolar composition under both impingement angles, which could be attributed to the combined role of both hardness and fracture toughness. Huang et al. studied the wear behavior of laser synthesized TiVCrAlSi HEA cladding on Ti6Al4V substrate [18]. The hardness of the cladding was found to be higher than substrate, which in turn lead to a huge improvement in wear resistance, and the primary reason behind this could be credited to the existence of hard silicide phase dissolved in a relatively ductile bcc matrix. Juan et al. [19] varied the Mo contribution in laser-coated $FeCrCoNiAlMo_x$ HEA on steel substrate and investigated its impact on the wear behavior. It was observed that 1% Mo contribution demonstrated higher wear resistance which was attributed to its superior mechanical properties. Similarly, $CoCrFeNiTi_x$ ($x=0, 0.5, 1$) HEA coatings on SS-904L proved to have better wear resistance than the substrate [20]. Wu et al. reveal the increase in wear resistance by addition of Al in $Al_xCoCrCuFeNi$ HEA and at the same time changing its wear mechanism from oxidation controlled to primarily delamination wear

[21]. Various findings demonstrated the ability of HEA to surpass conventionally preferred counterparts or the parent substrate material in the case of coating and claddings [22]. The corrosion behavior of HEAs has also been documented in various aqueous solutions [12, 23]. Research trends have shifted recently from equiatomic to non-equiatomic HEAs to explore ways to further enhance the corrosion resistance [24]. Furthermore, an effort is being made to realize the effect of element addition on the microstructural evolution and corrosion performance. HEA has shown quite high corrosion resistance based on the study performed by Huang et al. in which all three $CoCr_2Ni_2AlTi$, $Co_2Cr_2Ni_2AlTi$, and $CoCr_2Ni_3AlTi$ alloys prepared using vacuum arc melting furnace proved to be better than that of 304 stainless steel and other corrosion-resistant HEAs under 3.5 wt% NaCl solution or 0.5 M H_2SO_4 solution [25].

Refractory-based HEAs have attracted significant attention owing to their high strength and superior high-temperature properties. Particularly, the equimolar MoNbTaTiZr HEA composition has been recently investigated owing to its excellent hardness and corrosion resistance. MoNbTaTiZr HEA among other refractory alloys could be a feasible choice for enabling next-generation nuclear reactors, power generation, marine components, and material development and processing. Hua et al. performed a systematic investigation to find out microstructures, mechanical, corrosion, and wear behaviors of the $MoNbTaTi_xZr$ alloys. MoNbTaTiZr HEA exhibited a fine dendritic structure composed of two bcc solid solution phases, which lead to high hardness around 500 HV and yield strength of 1500 MPa [26]. It outperformed Ti6Al4V in the dry and wet wear test and demonstrated to have corrosion resistance nobler than that of the Ti6Al4V alloy, which indicates the relatively higher stability of the passivation film of the HEA. Furthermore, Perumal et al. performed stationary friction processing (SFP) a novel severe plastic deformation on MoNbTaTiZr, which led to significant elemental homogenization across dendritic and interdendritic regions in few minutes, similar to a week-long annealing treatment at 1275 K [12]. The processed alloy showed superior corrosion behavior due to the formation of a stable passive layer with zirconium oxide as the primary constituent and higher hydrophobicity. It also showed higher biocompatibility compared to its as-cast counterpart as well as conventional metallic biomaterials, including stainless steel (SS-316L) and titanium alloy (Ti6Al4V).

In the current work, slurry erosion and corrosion behavior of MoNbTaTiZr high-entropy alloy was investigated. For comparison, conventionally used structural materials SS316L stainless steel was tested under identical conditions. The HEA exhibited higher erosion–corrosion resistance as compared to stainless steel, which is primarily attributed to the higher hardness and superior corrosion resistance of the alloy.

2 Experimental Details

2.1 Materials and Characterization

An equimolar MoNbTaTiZr HEA was synthesized in vacuum arc melting from pure metal lumps (99.99% pure). The alloy was melted at least five times to ensure a uniform distribution of the constituent elements, and each melting was retained in a liquid state for at least 300 s. A wire electric discharge machine was used to cut HEA samples into 15 mm × 10 mm × 3 mm. All the samples were polished and grounded using abrasive papers down to 3000 grit size. Microstructural characterization of the samples was performed using scanning electron microscopy (SEM) images and X-ray diffraction (XRD). Both SS316L and HEA were subjected to hardness tests on a macro and microscale using Vickers indenter. Sand particles in size range of 75–150 μm were used for the slurry erosion studies (Fig. 1).

2.2 Slurry Erosion Test Rig

The re-circulation style test rig was used to carry out slurry erosion testing (Fig. 2). The test rig was made of a compressed air-driven diaphragm pump. The diaphragm pump is used to propel the premixed slurry in a container and forced to impinge on a sample via a 2-mm-diameter tungsten carbide nozzle. By adjusting the pressure of the compressed air, the velocity of the slurry jet is controlled. The test rig offers the flexibility to conduct experiments at a variety of different parameters, such as the angle of impingement, particle size, distance of stand-off, working

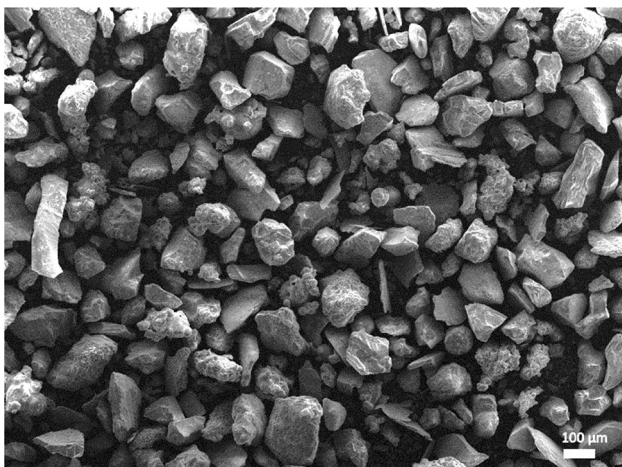


Fig. 1 Scanning electron microscopy (SEM) image of sand used

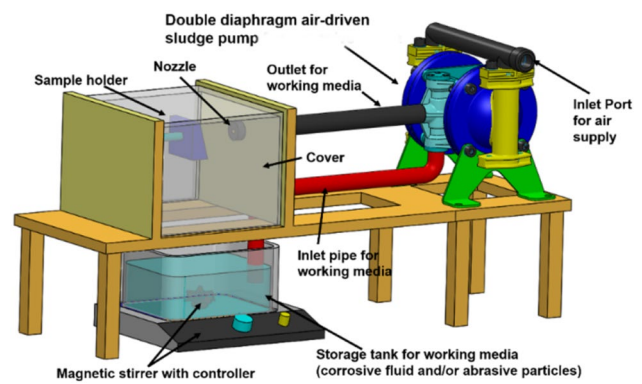


Fig. 2 Schematic illustrating the slurry erosion test rig used for experimentation [8]

media, and velocity of impact. The sedimentation of sand particles was prevented by continuous stirring.

2.3 Slurry Erosion Testing

In conjunction with the ASTM G-73 standard protocol, slurry erosion testing was performed. The slurry was prepared using river sand (75–150 μm), mixed with tap water, at a concentration of 5 kg m⁻³ (5000 ppm) (pH 7.72). A fresh batch of the slurry was prepared for each tested sample. Slurry erosion experiments were performed at a constant velocity of 20 m s⁻¹ for 2 h with samples positioned at different impingement angles, i.e., 30° and 90°. Gravimetric analysis was performed using a high precision weighing the balance of 0.01 mg resolution. Before weight measurement, samples were cleaned with acetone and dried using an air stream. The eroded surfaces were analyzed using a scanning electron microscope (SEM) to investigate the erosion mechanism.

2.4 Electrochemical Characterization

Electrochemical characterization of both SS316L and HEA was investigated using anodic polarization and electrochemical impedance spectroscopy (EIS) using the Gamry Interface 1000-E electrochemical setup. There is a three-electrode Gamry flat cell setup with saturated calomel electrode as reference electrode, pure graphite rod as counter electrode, and metal specimen as the working electrode in 3.5% NaCl solution. The anodic polarization was done at -0.3 V vs E_{OCP} to 1.0 vs E_{SCE} with the maximum allowed current density of 5 mA cm⁻². EIS curves were obtained at OCP from 0.01 Hz to 100 kHz frequency with an amplitude of 10 mV AC voltage. Experiments were performed in an open environment after 2 h of OCP stabilization. Gamry E-chem analyst 7.05 was used to model the equivalent electric circuit (EEC), and the simplex algorithm was used to fit the curve. SEM and 3D

profilometer images after corrosion analysis were captured and compared to distinguish the intensity of the pits.

3 Results and Discussion

3.1 Microstructural and Mechanical Characterization

The stainless steel used in this study is SS316L comprises of Fe, Cr, Ni, and few trace elements, whereas the HEA comprises equimolar composition of MoNbTaTiZr. The optical image of SS316L revealing its grain structure is shown in Fig. 3a. The average grain size of the SS316L was calculated to be approximately 22 μm . In contrast, microstructure of HEA is shown in Fig. 3b indicating the presence of two phases: major and minor bcc phases. In addition, no secondary phase has been found in MoNbTaTiZr HEA. Thin dendrites illustrate major bcc phase with darker contrast, and the interdendritic region with brighter contrast depicts the minor bcc phase. XRD analysis of both the alloys is shown in Fig. 4. SS316 primarily shows the presence of austenite with fcc structure, while HEA shows the presence of a dual-phase structure, comprising of major and minor bcc phases. The major bcc phase was found to be approximately $\sim 30\%$ using phase-contrast images. The lattice parameters for both the phases were determined using the Bragg's equation and miller indices (321 plane) [27]. It is reported to be 0.3310 nm for the major bcc phase and 0.3379 nm for the minor bcc phase. The severe segregation of the MoNbTaTiZr can be described due to the difference in the melting temperatures of the individual elements (Fig. 5). Zr and Ti tend to stay together which is of lower melting point (T_m) and form a minor bcc phase (inter-dendritic region), whereas higher melting elements (T_m) such as Ta, Mo, and Nb tend to form a major bcc phase (dendritic region). Further, the phase separation of Zr–Ta happens generally at 2020 K to individually rich phases of Zr and Ta [27]. It might add on to the reason of severe segregation in this alloy. In addition, a very high affinity between Ti and Zr due to approximately zero mixing enthalpy between them favors the minor bcc phase formation. The chemical composition of the dendritic and interdendritic phases was approximated using EDS analysis as $\text{Mo}_{24}\text{Nb}_{20}\text{Ta}_{31}\text{Ti}_{15}\text{Zr}_{10}$ and $\text{Mo}_{13}\text{Nb}_{12}\text{Ta}_8\text{Ti}_{24}\text{Zr}_{43}$, respectively. Thus, the dendritic region in the as-cast HEA is primarily composed of Ta, Nb, and Mo, while the interdendritic region contains Ti and Zr as the major elements. The relatively high melting temperature elements, including Ta, Nb, and Mo, solidify first during cooling down and grew into the dendritic structure, while lower melting temperature elements, i.e., Ti and Zr, are pushed into interdendritic regions. In terms of hardness, SS-316L is reported to be 3.3 GPa on Vickers hardness scale, whereas MoNbTaTiZr HEA

is reported to be 4.9 GPa (macroscale). The individual hardness of the dendritic and interdendritic region was reported to be 6.4 GPa and 5.7 GPa (microscale), respectively. Thus, in comparison with SS316L, HEA has the advantages of being significantly harder and has the potential to sustain detrimental erosion–corrosion during marine applications.

3.2 Slurry Erosion–Corrosion Behavior

Slurry erosion and erosion–corrosion results of the SS316L and MoNbTaTiZr HEA are shown in Fig. 6. Results indicate lower erosion rates for the HEA compared to the conventionally used SS316L steel under oblique conditions. Under erosive conditions, the HEA showed two times higher erosion resistance than the stainless steel during the oblique impact condition. However, the erosion rates slightly increased under the normal impact condition with values slightly higher than the stainless steel. A similar trend was also observed under erosion–corrosion conditions with significantly high erosion–corrosion resistance exhibited by the HEA, which was more than 3.5 times higher than the stainless steel. These results indicate a brittle erosion mode for the HEA, whereas a ductile response for the SS316L. For both materials, the material removal rate increased with the introduction of the corrosive media into the slurry. However, it is interesting to note that, irrespective of the impact angle, the HEA showed minimal positive synergy compared to the stainless steel highlighting high corrosion resistance. In the case of stainless steel, the erosion rates at the oblique angle increased by two times during erosion–corrosion conditions when compared with the erosion under similar conditions. However, the HEA showed less than 10% rise in the erosion rates when tested under the erosion–corrosion conditions. The higher erosion and erosion–corrosion resistance of the HEA than stainless steel at the oblique conditions is dominantly related to the higher hardness. On a macroscale, the HEA showed 50% higher hardness, whereas at the microscale, the hardness was two times higher than that of the stainless steel. Due to higher hardness, the resistance to the shearing and plastic deformation of the material by the abrasive particles is increased. The abrasive particle impacting at the oblique angle tends to indent the target material as a result of the normal velocity component. Thereafter, shearing of the target material is initiated aided by the tangential velocity component. The high target material hardness limits the indentation and shearing phenomena lowering the removal of the material. Further, the presence of a dendritic structure of higher hardness also lowers the removal of the material by limiting the motion of the abrasive particles during the shearing action. Such composite structures provide higher protection against

Fig. 3 The optical microscopy images showing the microstructure of **a** SS316L stainless steel and **b** MoNbTaTiZr high-entropy alloy

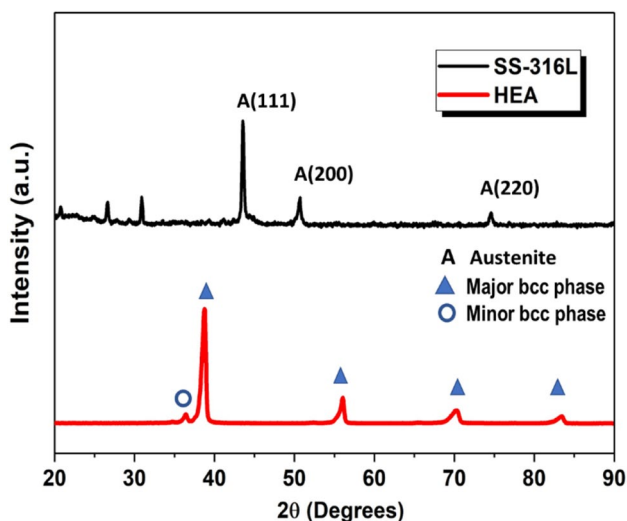
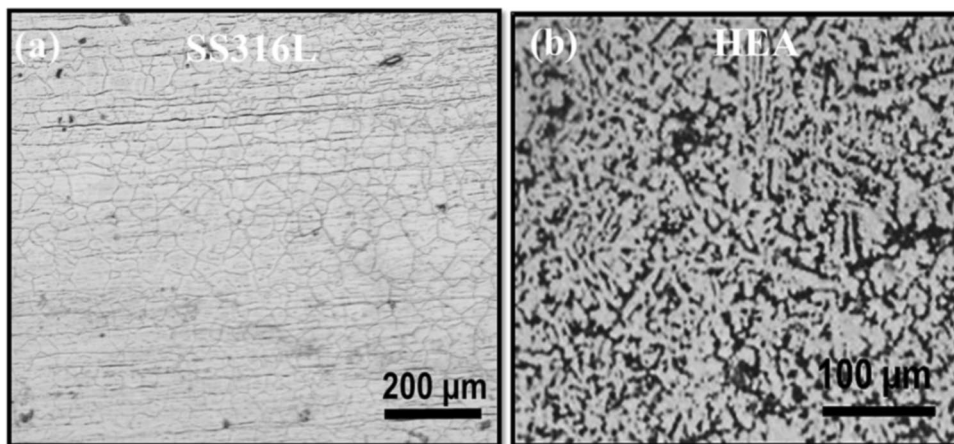


Fig. 4 X-ray diffraction (XRD) patterns of developed MoNbTaTiZr Alloy and SS-316L

erosion at the oblique angles [28]. On the contrary, during the normal impingement of the abrasive particles, the materials removal process is dominantly controlled by the toughness and the resistance to the plastic deformation. In the case of the ductile material, the impact of particles at the normal impact results in the formation of the extruded platelets, which finally detach due to subsequent impact [29, 30]. However, for the brittle materials, impacts follow an extensive cracking and spalling of the material. This explains the higher resistance of the stainless steel during the erosion and erosion–corrosion phenomena. Compared to the HEA, the stainless steel possessed higher toughness as measured using the indentation technique. The presence of cracks was observed in case of the HEA, while no such cracking was visible in the case of the stainless steel. The SEM images of the eroded surfaces shown in Fig. 7 also highlight similar behavior. For both stainless steel and the HEA, the eroded surface showed

Fig. 5 Energy-dispersive spectroscopy (EDS) mapping of the elements in the as-cast MoNbTaTiZr high-entropy alloy for the phase-specific composition analysis at dendritic and interdendritic regions

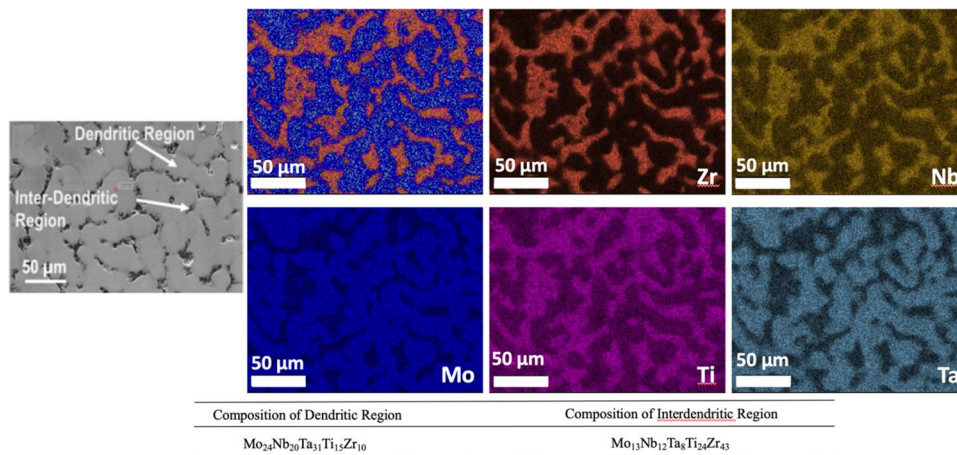


Fig. 6 **a** Hardness of the specimen and **b** slurry erosion (SE) and slurry erosion–corrosion (SEC) results for the SS316L steel and MoNbTaTiZr high-entropy alloy tested at impingement angles of 30° and 90°

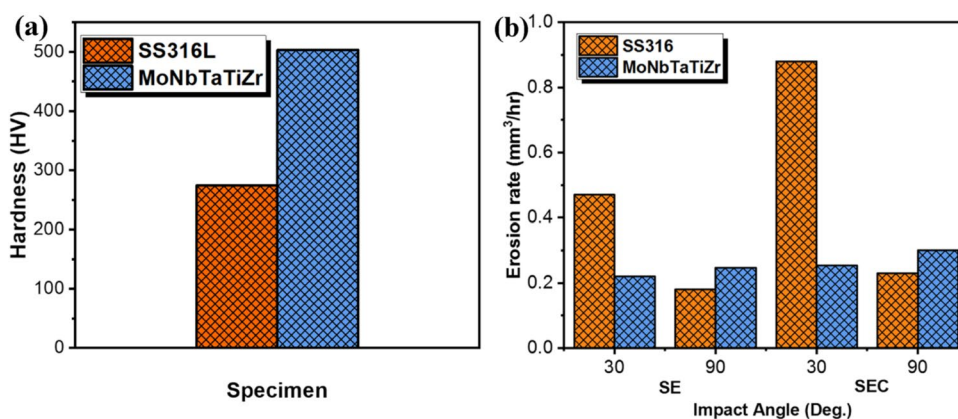
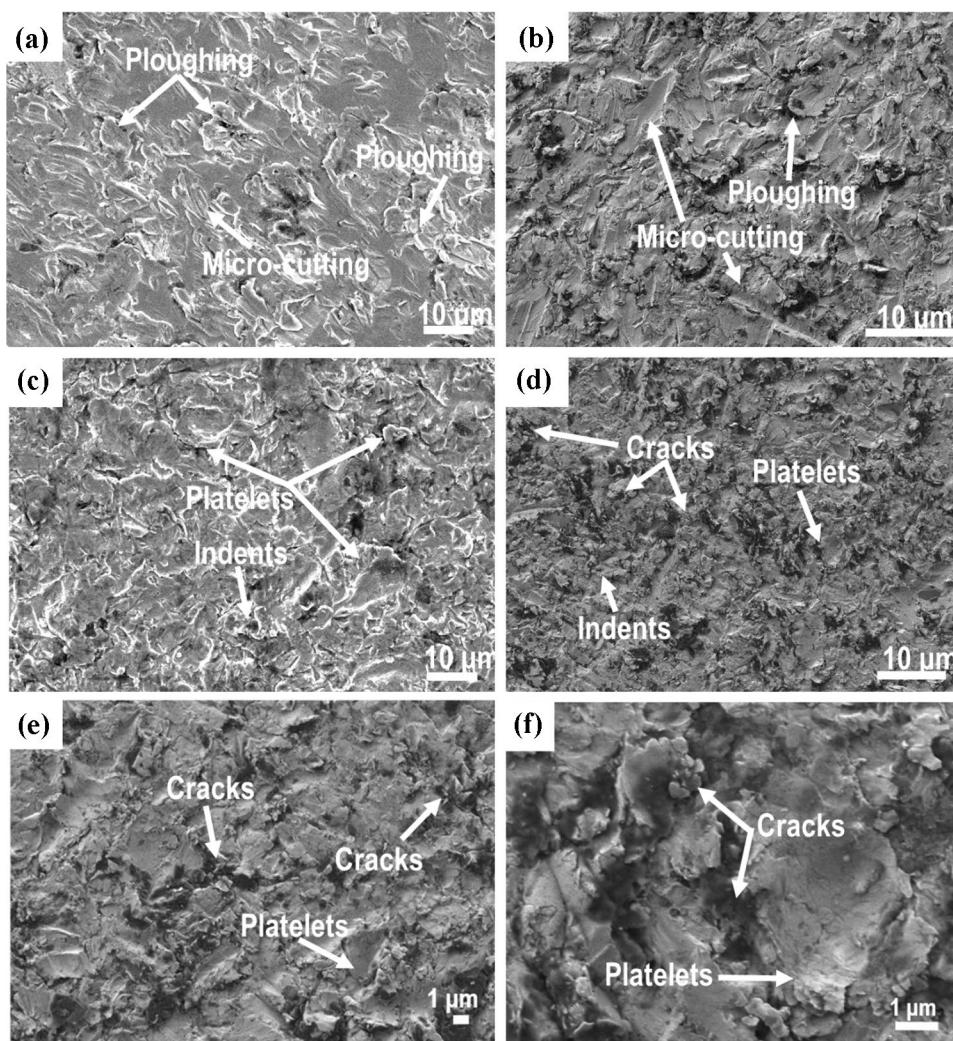


Fig. 7 SEM image of surface after slurry erosion of **a** SS-316L at 30°, **b** MoNbTaTiZr at 30°, **c** SS-316L at 90°, and **d–f** MoNbTaTiZr at 90° impingement angles



the presence of micro-cutting and ploughing with higher severity in the case of the former. This illustrates the better performance of the HEA under oblique conditions. However, for the normal impact conditions, the eroded surface of the stainless steel was composed of extensively

extruded platelets. In the case of the HEA, in addition to the platelets, the eroded surface also showed the presence of cracks, especially in the interdendritic region (Fig. 7d–f). The hardness of these interdendritic regions was higher side than the dendritic counterpart indicating

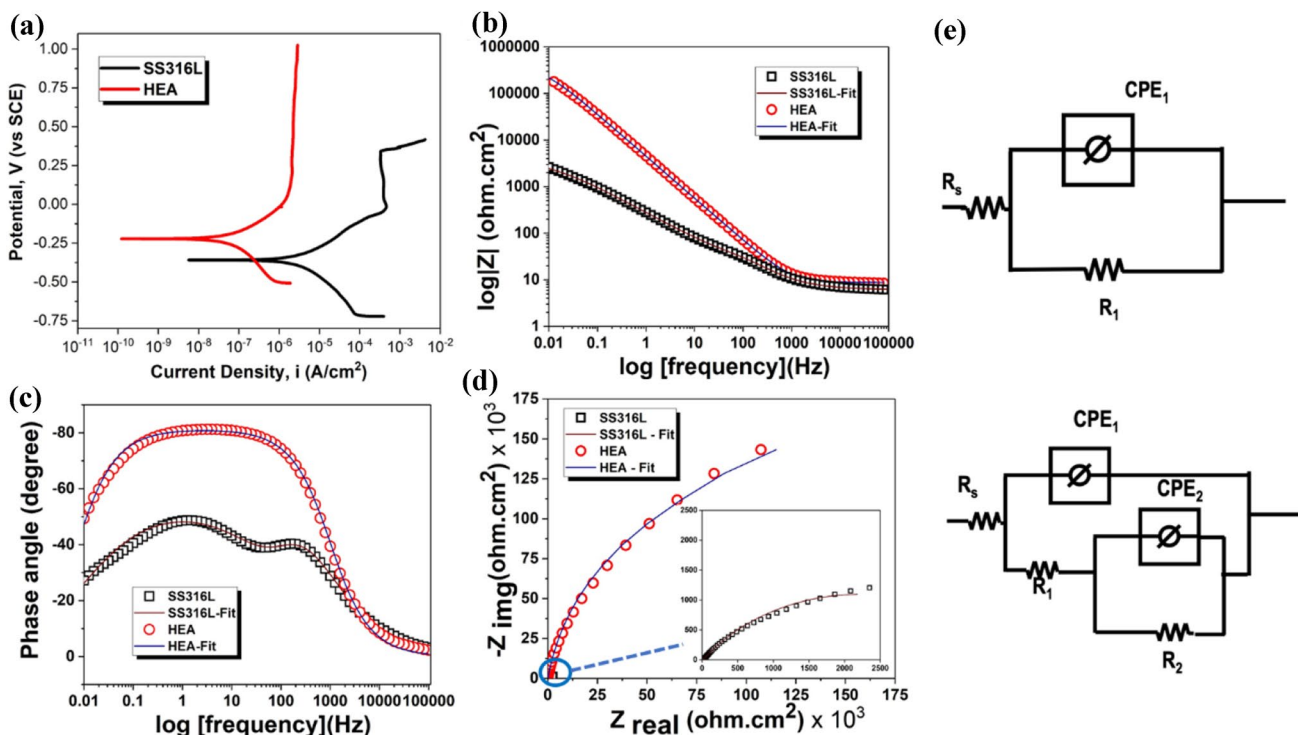


Fig. 8 a Potentiodynamic curves, b Bode magnitude plot, c Bode phase angle plot, d Nyquist curves of the as-cast MoNbTaTiZr alloy and SS-316L obtained from electrochemical impedance spectroscopy (EIS) in 1 mol NaCl solution, and e electrical equivalent circuits (EECs) used to fit the obtained results. Inset images in panel d show the zoomed-in region

Table 1 Corrosion current density (I_{corr}), corrosion potential (E_{corr}), and corrosion per year (mpy) obtained from the potentiodynamic curve

Sample	I_{corr} ($\mu\text{A cm}^{-2}$)	E_{corr} (mV)	Corrosion rate	E_{pit} (mV)
SS316L	7.710	-359	3.47600	320
HEA	0.096	-222	0.02985	NA

the presence of high brittleness. Thus, the HEA showed a mixed response with ductile–brittle erosion behavior being modulated by the presence of dual-phase microstructure. Further, in addition to hardness, the minimal positive synergy exhibited by the HEA also contributed in enhancing the resistance to erosion–corrosion. The electrochemical behavior of both SS316L and MoNbTaTiZr HEA is shown in Fig. 8. The potentiodynamic behavior of these alloys was investigated in 3.5% NaCl at 37 °C. The obtained corrosion parameters are shown in Table 1. E_{corr} (corrosion potential, the equilibrium potential during the potential sweep where the current changes its sign from cathodic to anodic) is higher for HEA, indicating superior passive behavior and nobler nature. Similarly,

I_{corr} (corrosion current density, obtained after Tafel fitting of the curves at E_{corr}) of HEA was reported to 80 times lower compared to stainless steel. It shows the superiority of the HEA compared to stainless steel in an aqueous corrosion environment. In general, most of the metals in marine or aqueous environments fail due to pitting corrosion [31, 32]. Thus, the pitting potential (at which the current density sharply increases) of the specimens was calculated using a potentiodynamic polarization study. SS-316L started pitting at around 320 mV (vs SCE) and the SEM and 3D profilometer image of the pitted sample is shown in Fig. 9a–d. The profilometer images illustrate wide and deep pits of around 800 μm and 200 μm formed on SS after potentiodynamic polarization tests, whereas no sign of pit was observed on HEA (Fig. 9e, f). In contrast, the HEA did not show any pitting behavior, unlike the stainless steel as observed during the potentiodynamic plots (Fig. 8a). This is due to the fact that HEA spontaneously forms the thick passive layer as soon as it comes in contact with the aqueous medium. This is due to the presence of Zr, Nb, and Ta as an alloying element which tends to form highly corrosion-resistant TiO_2 , ZrO_2 , Nb_2O_5 rapidly upon being in contact with electrolyte as has been observed in XPS results [12]. The Nyquist plot

Table 2 Electrochemical parameters obtained from the electrochemical impedance spectroscopy (EIS) study

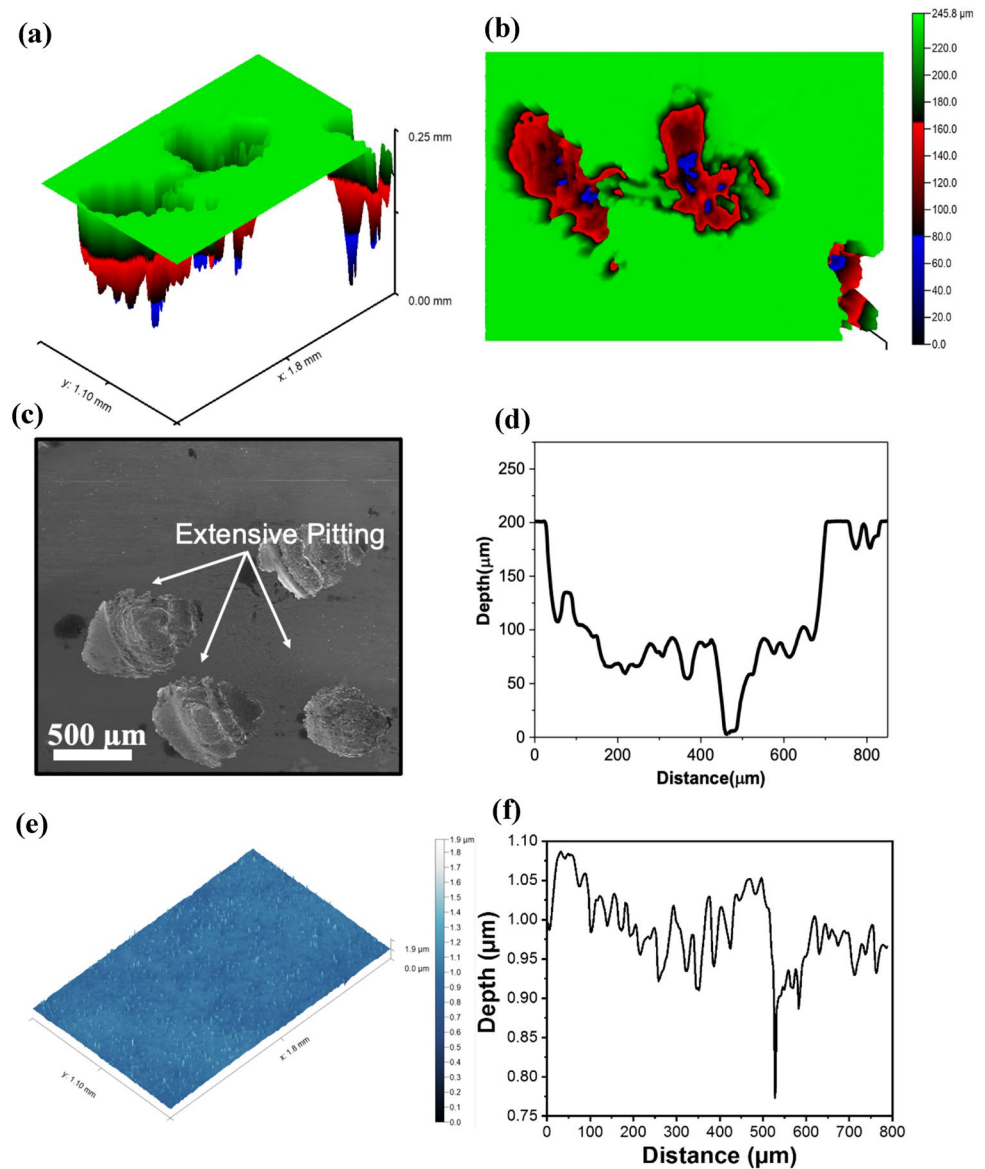
Sample	R_1 (kohm cm ²)	R_2 (kohm cm ²)	R_p (kohm cm ²)	CPE_1 ($\mu\text{S s}^n$ cm ⁻²)	n_1	CPE_2 ($\mu\text{S s}^n$ cm ⁻²)	n_2	Total CPE ($\mu\text{S s}^n R_s$ (kohm cm ²) cm ⁻²)	Goodness of fit
SS316L	1.510	3.985	5.495	280.400	0.718	943.400	0.589	1223.80	0.810×10^{-3}
HEA	382.1	–	382.1	42.08	0.903	–	–	42.08	0.567×10^{-3}

obtained using the EIS study is shown in Fig. 8d with the values of different parameters obtained after circuit fitting shown in Table 2. The circuits used to fit the experimental values are shown in Fig. 8e. The bigger impedance spectra obtained in the case of HEA are an indication of superior passive layer response by the specimen. In contrast, stainless steel showed very low impedance spectra of polarization resistance of 5 kohm cm². Also, the higher impedance obtained for HEA is clearly evident from the frequency-Bode plot. The phase angle Bode plot indicates there is only a one time step for HEA, whereas SS showed multiple time steps. Thus, this explains the rationale of using two RC circuits used to fit the obtained values for SS. Further, the n factor used during the fitting of the obtained curves in CPE element denotes the surface inhomogeneities on the passive layer. Thus, the higher value of 0.9 for HEA compared to 0.71 of SS suggests a dense and stable passive layer formed for the HEA. Overall, in the aspect of erosion–corrosion, the MoNbTaTiZr HEA under marine environment showed superior performance to that of the stainless steel.

4 Conclusion

In the present work, the slurry erosion–corrosion behavior of the developed MoNbTaTiZr high-entropy alloy (HEA) was investigated at different impingement conditions. For comparison, the performance of the conventionally used SS316L steel was also investigated. The microstructural analysis of HEA reported both major bcc and minor bcc phases, whereas SS316L was found to be fcc austenite with a grain size of 22 μm . In terms of hardness, HEA reported approximately 1.5 times higher value on the Vickers scale compared to SS316L. Under slurry erosion–corrosion conditions, the HEA showed more than 3.5 times higher erosion resistance than the stainless steel at the oblique impact conditions. The performance of the HEA was nevertheless similar to that of the stainless steel under normal impingement conditions. Overall, the HEA showed a mixed ductile–brittle response compared to the ductile mode of erosion observed for the stainless steel. The better performance of the HEA is related to high hardness and exceptionally high corrosion resistance. The HEA showed 80 times lower current density than the stainless steel in 3.5% NaCl solution. This resulted in a mild positive synergy and high erosion–corrosion resistance. The developed HEA is a potential candidate for use in engineering components being subjected to severe slurry erosion–corrosion conditions.

Fig. 9 a–d Surface profilometer and scanning electron microscopy images showing the pitting of SS-316L after corrosion and e and f surface profilometer of the corroded MoNbTaTiZr surface



Funding Not applicable.

Data Availability On request.

Declarations

Conflict of interest Authors declare no conflict of interest.

References

1. Javaheri V, Porter D, Kuokkala V-T (2018) Slurry erosion of steel—review of tests, mechanisms and materials. *Wear* 408–409:248–273
2. Arora HS, Rani M, Perumal G, Singh H, Grewal HS (2020) Enhanced cavitation erosion–corrosion resistance of high-velocity oxy-fuel-sprayed Ni–Cr–Al₂O₃ coatings through stationary friction processing. *J Therm Spray Technol* 29:1183–1194
3. Babu A, Arora H, Singh R, Grewal H (2021) Slurry erosion resistance of microwave derived Ni–SiC composite claddings. *Silicon*. <https://doi.org/10.1007/s12633-020-00849-9>
4. Santa J, Espitia L, Blanco J, Romo S, Toro A (2009) Slurry and cavitation erosion resistance of thermal spray coatings. *Wear* 267:160–167
5. Murty BS, Yeh J-W, Ranganathan S, Bhattacharjee P (2019) High-entropy alloys. Elsevier, Amsterdam
6. Yeh JW, Chen YL, Lin SJ, Chen SK (2007) High-entropy alloys—a new era of exploitation. *Mater Sci Forum* 560:1–9
7. Cantor B (2014) Multicomponent and high entropy alloys. *Entropy* 16:4749–4768
8. Nair RB, Selvam K, Arora HS, Mukherjee S, Singh H, Grewal HS (2017) Slurry erosion behavior of high entropy alloys. *Wear* 386–387:230–238

9. Garg M, Grewal H, Arora H (2021) Effect of microwave processing on the oxidation behavior of refractory high entropy alloy. *Mater Chem Phys* 262:124256
10. Shen H, Zhang J, Hu J, Zhang J, Mao Y, Xiao H, Zhou X, Zu X (2019) A novel TiZrHfMoNb high-entropy alloy for solar thermal energy storage. *Nanomaterials* 9:248
11. Sadeghilaridjani M, Ayyagari A, Muskeri S, Hasannaemi V, Salloom R, Chen W-Y, Mukherjee S (2020) Ion irradiation response and mechanical behavior of reduced activity high entropy alloy. *J Nucl Mater* 529:151955
12. Perumal G, Grewal HS, Pole M, Reddy LVK, Mukherjee S, Singh H, Manivasagam G, Arora HS (2020) Enhanced biocorrosion resistance and cellular response of a dual-phase high entropy alloy through reduced elemental heterogeneity. *ACS Appl Biomater* 3:1233–1244
13. Gludovatz B, Hohenwarter A, Catoor D, Chang EH, George EP, Ritchie RO (2014) A fracture-resistant high-entropy alloy for cryogenic applications. *Science* 345:1153–1158
14. Senkov O, Wilks G, Miracle D, Chuang C, Liaw P (2010) Refractory high-entropy alloys. *Intermetallics* 18:1758–1765
15. Zhang Y, Zuo TT, Tang Z, Gao MC, Dahmen KA, Liaw PK, Lu ZP (2014) Microstructures and properties of high-entropy alloys. *Prog Mater Sci* 61:1–93
16. Nair RB, Arora HS, Grewal HS (2020) Slurry erosion–corrosion of bimodal complex concentrated alloy composite cladding. *Adv Eng Mater* 22:2000626
17. Nair RB, Arora HS, Mandal P, Das S, Grewal HS (2018) High-performance microwave-derived multi-principal element alloy coatings for tribological application. *Adv Eng Mater* 20:1800163
18. Huang C, Zhang Y, Vilar R, Shen J (2012) Dry sliding wear behavior of laser clad TiVCrAlSi high entropy alloy coatings on Ti–6Al–4V substrate. *Mater Des* 41:338–343
19. Juan Y, Li J, Jiang Y, Jia W, Lu Z (2019) Modified criteria for phase prediction in the multi-component laser-clad coatings and investigations into microstructural evolution/wear resistance of FeCrCoNiAlMo_x laser-clad coatings. *Appl Surf Sci* 465:700–714
20. Guo Y, Shang X, Liu Q (2018) Microstructure and properties of in-situ TiN reinforced laser cladding CoCr₂FeNiTi_x high-entropy alloy composite coatings. *Surf Coat Technol* 344:353–358
21. Wu J-M, Lin S-J, Yeh J-W, Chen S-K, Huang Y-S, Chen H-C (2006) Adhesive wear behavior of Al_xCoCrCuFeNi high-entropy alloys as a function of aluminum content. *Wear* 261:513–519
22. Li W, Liu P, Liaw PK (2018) Microstructures and properties of high-entropy alloy films and coatings: a review. *Mater Res Lett* 6:199–229
23. Nene S, Frank M, Liu K, Sinha S, Mishra R, McWilliams B, Cho K (2019) Corrosion-resistant high entropy alloy with high strength and ductility. *Scr Mater* 166:168–172
24. Zhang W, Liaw PK, Zhang Y (2018) Science and technology in high-entropy alloys. *Sci China Mater* 61:2–22
25. Huang L, Wang X, Zhao X, Wang C, Yang Y (2021) Analysis on the key role in corrosion behavior of CoCrNiAlTi-based high entropy alloy. *Mater Chem Phys* 259:124007
26. Hua N, Wang W, Wang Q, Ye Y, Lin S, Zhang L, Guo Q, Brechtel J, Liaw PK (2020) Mechanical, corrosion, and wear properties of biomedical Ti–Zr–Nb–Ta–Mo high entropy alloys. *J Alloys Compd* 861:157997
27. Wang S-P, Xu J (2017) TiZrNbTaMo high-entropy alloy designed for orthopedic implants: as-cast microstructure and mechanical properties. *Mater Sci Eng C* 73:80–89
28. Hutchings I, Shipway P (2017) Tribology: friction and wear of engineering materials, 2nd edn. Butterworth-Heinemann, Cambridge, pp 37–77
29. Grewal HS, Agrawal A, Singh H (2013) Slurry erosion mechanism of hydroturbine steel: effect of operating parameters. *Tribol Lett* 52:287–303
30. Grewal HS, Agrawal A, Singh H (2013) Slurry erosion performance of Ni–Al₂O₃ based composite coatings. *Tribol Int* 66:296–306
31. Selvam K, Saini J, Perumal G, Ayyagari A, Salloom R, Mondal R, Mukherjee S, Grewal HS, Arora HS (2019) Exceptional cavitation erosion–corrosion behavior of dual-phase bimodal structure in austenitic stainless steel. *Tribol Int* 134:77–86
32. Tan L, Wang Z, Ma Y (2021) Tribocorrosion behavior and degradation mechanism of 316L stainless steel in typical corrosive media. *Acta Metall Sin (Engl Lett)*. <https://doi.org/10.1007/s40195-020-01182-1>

Publisher's Note Springer Nature remains neutral with regard to jurisdictional claims in published maps and institutional affiliations.